

Glassy swirls of active dumbbells

Rituparno Mandal,^{1,*} Pranab Jyoti Bhuyan,^{1,†} Pinaki Chaudhuri,^{2,‡} Madan Rao,^{3,§} and Chandan Dasgupta^{1,||}

¹Centre for Condensed Matter Theory, Department of Physics, Indian Institute of Science, Bangalore 560012, India

²The Institute of Mathematical Sciences, Chennai 600113, India

³Simons Centre for the Study of Living Machines, National Centre for Biological Sciences (TIFR), Bangalore 560065, India

(Received 10 March 2017; revised manuscript received 25 September 2017; published 13 October 2017)

Is an active glass different from a conventional passive glass? To address this, we study the dynamics of a dense binary mixture of soft dumbbells, each subject to an active propulsion force and thermal fluctuations. This dense assembly shows dynamical arrest, first to a translational and then to a rotational glass, as one reduces temperature T or the self-propulsion force f . We monitor the dynamics along an iso-relaxation-time contour in the $(T-f)$ plane. We find dramatic differences both in the fragility and in the nature of dynamical heterogeneity, which characterize the onset of glass formation—the activity-induced glass exhibits large swirls or vortices, whose scale is set by activity, and it appears to diverge as one approaches the glass transition. This large collective swirling movement should have implications for collective cell migration in epithelial layers. We construct continuum hydrodynamic equations for the simulated system, and we show that the observed behavior of this growing dynamic length scale can be understood from these equations.

DOI: [10.1103/PhysRevE.96.042605](https://doi.org/10.1103/PhysRevE.96.042605)

I. INTRODUCTION

Assemblies of self-propelled objects jam at high densities [1–4] and low temperatures [5]. On approaching dynamical arrest from the fluid side, these dense active assemblies are seen to exhibit typical glassy dynamics, with activity manifesting simply as an *effective temperature* [5,6]. Likewise, starting from the jammed state, activity is seen to prematurely *fluidize* the system at a reduced (enhanced) transition temperature (volume fraction) [1–5]. On the face of it, it might appear that an active glass behaves very similarly to a conventional one, albeit with a different effective temperature or density [1,6]. In this paper we provide evidence to the contrary, i.e., we show that an active glass of anisotropic objects exhibits distinctive dynamical features that are qualitatively different from those of its passive counterpart.

We consider dense assemblies of generic oriented nonspherical self-propelled objects [7–12], which are free to explore both translational and orientational degrees of freedom. Our rationale for such a system is that radical departures from equilibrium are manifest when the self-propelled particles are made anisotropic [13–15]. Living realizations include reconstituted layer of confluent epithelial cells [16], where cell shape anisotropy plays a crucial role in the jamming-unjamming transition [17], and jammed biofilms formed by a dense collection of rod-shaped bacteria [18]. Shaken nonspherical grains at high packing densities constitute nonliving examples [19].

We perform Brownian dynamics simulations of a dense binary assembly of dumbbells [20–23] in two dimensions; the 50:50 mixture of A - and B -type dumbbells with a number density $\rho = 1.6$ ensures amorphous steady-state structures. This assembly, subject to a temperature bath T , is made active

by driving each dumbbell with a body-fixed propulsion force f along the long axis of each dumbbell, and it is characterized by a Peclet number $Pe \equiv f\sigma_{AA}/k_B T$, measuring the relative strength of activity with respect to temperature [7,12].

We show that the phase diagram of such a model system exhibits a dynamically arrested state upon reducing either temperature or self-propulsion force. Our main result is that the dynamical signatures of an active glass are fundamentally different from a conventional glass: (i) activity makes the glass less fragile, and (ii) the nature of dynamical heterogeneity in an active glass is very unique and exhibits large-scale swirls and vortices, whose size increases and appears to diverge as one approaches the arrested state by reducing the self-propulsion force f . We construct continuum hydrodynamic equations for the assembly of active dumbbells, and we show that these equations provide a complete understanding of the observed behavior of this growing dynamic length scale. These large-scale swirls are the sluggish imprints of the collective turbulent motion observed in an active fluid of anisotropic particles [9,10,24] at lower densities.

The rest of the paper is organized as follows. In Sec. II, we discuss the model system, the numerical simulation method, and the various dynamical measures used. In Sec. III, we report the results of our numerical simulations in the dilute and dense regimes of the model. In Sec. IV, we discuss the hydrodynamic model for the assembly of active dumbbells, and we provide a detailed discussion of the emergence and growth of the dynamical length scales observed in our numerical simulations. We end with some concluding remarks in Sec. V.

II. MODEL AND SIMULATION DETAILS

In this section, we describe our Brownian dynamics simulation of a two-dimensional binary dumbbell mixture. Each dumbbell consists of two spherical monomers of the same type (either A or B) connected via a spring with a stiffness of $k = 200$; a schematic of the dumbbell is illustrated in the inset of Fig. 1(a). This value of spring constant makes the

*rituparno@physics.iisc.ernet.in

†pranab@physics.iisc.ernet.in

‡pinakic@imsc.res.in

§madan@ncbs.res.in

||cdgupta@physics.iisc.ernet.in

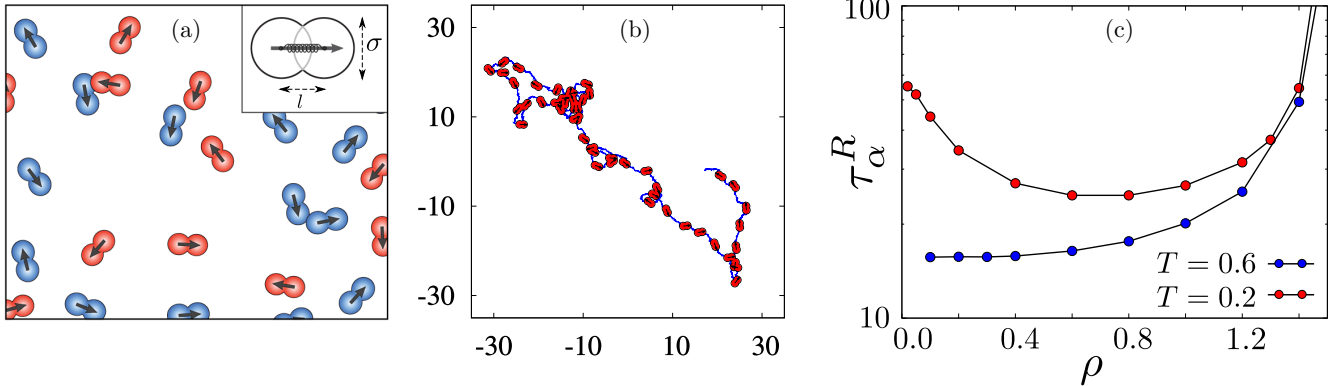


FIG. 1. (a) Binary assembly of self-propelled dumbbells of A (blue) or B (red) type in the dilute limit, built from two identical soft Lennard-Jones (LJ) spheres of diameter σ connected through a harmonic spring of stiffness k and rest length l (inset). The body-fixed self-propulsion force f (arrow) is along the long axis of each dumbbell. (b) Stochastic trajectory of a single active dumbbell in the dilute regime ($\rho = 0.1$) at $T = 0.5$, in the presence of an active force ($f = 5$), showing center-of-mass position and dumbbell orientation. (c) Rotational correlation time τ_α^R vs density ρ for the assembly of active dumbbells for $f = 10.0$ at two temperatures, $T = 0.2$ (red) and $T = 0.6$ (blue). Orientational decorrelation happens because of both thermal fluctuations and collisions as a consequence of active and thermal driving. We see that at $T = 0.6$, the rotational persistence time increases monotonically with density; this is because rotational fluctuations are hindered due to crowding. At $T = 0.2$, however, τ_α^R decreases at first from a high value before increasing again; this initial decrease with density arises from the increasing number of collisions encountered by persistent dumbbells.

dumbbells fairly rigid with an equilibrium length $l = \sigma_{\alpha\alpha}/2$ (where $\alpha \in A, B$) between the centers of the two monomers of each dumbbell [7,12,21]. The mixture consists of 50:50 A-A and B-B dumbbells, which leads to amorphous structures. The equation of motion for each monomer can be written as

$$\dot{\mathbf{r}}_i = \frac{1}{\gamma} \left[\sum_{\{ij\}} \mathbf{f}_{ij} - k(\mathbf{r}_i - \mathbf{r}_{i'} - l\mathbf{n}_i) + f\mathbf{n}_i \right] + \boldsymbol{\eta}_i, \quad (1)$$

where γ is the friction coefficient, \mathbf{f}_{ij} is the interaction force between the i th and the j th monomer, i and i' denote the two monomers of the same dumbbell, \mathbf{n}_i is the unit vector in a prespecified direction along the long axis of the dumbbell associated with the i th particle, f is the strength of the propulsion force, and $\boldsymbol{\eta}_i$ is the thermal noise, which satisfies the fluctuation-dissipation relation of the form $\langle \boldsymbol{\eta}_i(t) \cdot \boldsymbol{\eta}_i(t') \rangle = 2D\delta(t - t')$ with $\langle \boldsymbol{\eta}_i(t) \rangle = 0$, $D = \frac{k_B T}{\gamma}$; T is the temperature of the heat bath. The interaction force (\mathbf{f}_{ij}) between the monomers is modeled via the Lennard-Jones pair potential,

$$V_{ij}(r) = 4\epsilon_{\alpha\beta} \left[\left(\frac{\sigma_{\alpha\beta}}{r_{ij}} \right)^{12} - \left(\frac{\sigma_{\alpha\beta}}{r_{ij}} \right)^6 \right], \quad (2)$$

where r_{ij} is the distance between the i th and the j th particle, i.e., $r_{ij} = |\mathbf{r}_i - \mathbf{r}_j|$, where α and β represent either A-type or B-type particles. In our simulation, we have chosen the values of $\sigma_{\alpha\beta}$ and $\epsilon_{\alpha\beta}$ to be $\sigma_{AB} = 0.8\sigma_{AA}$, $\sigma_{BB} = 0.88\sigma_{AA}$, $\epsilon_{AB} = 1.5\epsilon_{AA}$, and $\epsilon_{BB} = 0.5\epsilon_{AA}$. The potential has been truncated at $r_{\alpha\beta}^c = 2.5\sigma_{\alpha\beta}$ and the potential has been shifted accordingly such that both the potential and the force are continuous at the cutoff. The unit of length and energy in our simulation are set by $\sigma_{AA} = 1$ and $\epsilon_{AA} = 1$ and the study is done for an overall number density of $\rho = 1.6$.

The Brownian dynamics updates are done using the Euler algorithm. The number of integration steps for the simulation

is between 10^8 and 10^9 depending on the parameters with a time step of integration $dt = 10^{-3}$. We have compared our Brownian dynamics results to those of Newtonian dynamics simulations and observed that the long time dynamics is quantitatively similar for the parameter ranges we have studied, as expected. For each parameter set, the results presented here have been averaged over 16–32 independent trajectories.

To identify the onset of translational and rotational glassy behavior in the $(T-f)$ plane, we monitor the following quantities: (i) the translational and rotational mean-square displacements (MSD), $\langle \Delta \mathbf{r}(t)^2 \rangle = \langle \frac{1}{N} \sum_i |\mathbf{r}_i(t_0 + t) - \mathbf{r}_i(t_0)|^2 \rangle$ and $\langle \Delta \theta(t)^2 \rangle = \langle \frac{1}{N} \sum_i [\theta_i(t_0 + t) - \theta_i(t_0)]^2 \rangle$, where \mathbf{r}_i and θ_i are the center-of-mass and orientation of the i th dumbbell; (ii) the orientation correlation function $C_2(t) = \frac{1}{N} \sum_i \langle P_2[\mathbf{n}_i(t_0) \cdot \mathbf{n}_i(t_0 + t)] \rangle$ [21,22], where P_2 is the second-order Legendre polynomial and \mathbf{n}_i is the unit vector along the long axis of the i th dumbbell; and (iii) the overlap function $Q(t) = \langle \frac{1}{N} \sum_i w[|\mathbf{r}_i(t_0) - \mathbf{r}_i(t_0 + t)|] \rangle$, where $w(r) = 1$ if $r \leq a$ and 0 if $r > a$, with $a = 0.3$ [25]. Here, $\langle \dots \rangle$ denotes an average over time origins t_0 and trajectories, and N is the number of dumbbells. From the measured time correlation functions, $C_2(t)$ and $Q(t)$, we estimate the corresponding rotational and translational α -relaxation time scales, τ_α^R and τ_α^T , respectively, by noting the time at which each of the functions decays to a value of $1/e$.

III. SIMULATION FINDINGS AND ANALYSIS

A. Active dumbbells at low density

We first note that in our model, *activity* is introduced via a self-propulsion force of magnitude f that acts on each monomer, of each dumbbell, in a prespecified direction along the corresponding dumbbell axis. Therefore, although each dumbbell consists of two identical beads and hence is structurally apolar, the self-propulsion force endows each

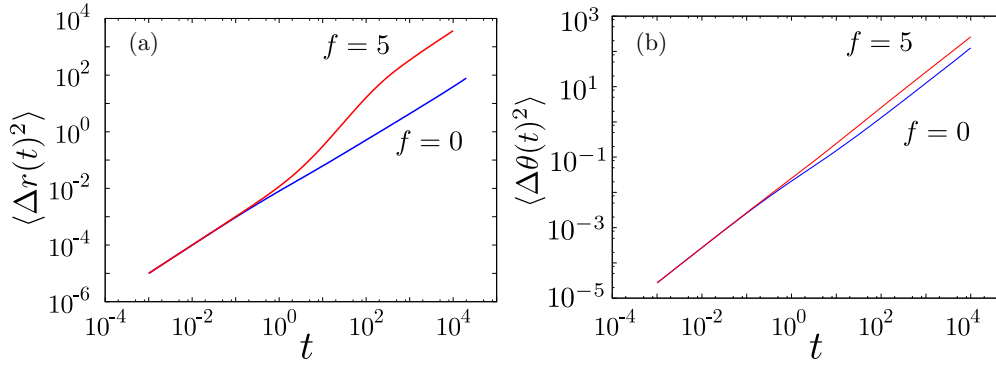


FIG. 2. The translational and rotational mean-square displacement (MSD) of a single active dumbbell in the dilute regime ($\rho = 0.1$) at $T = 0.5$, with and without an active force, $f = 0$ and 5 , respectively.

dumbbell with a polar vector. Each dumbbell is in contact with a thermal heat bath of temperature T , which enters in our Langevin simulation [Eq. (1)] as the strength of the thermal noise obeying the fluctuation-dissipation theorem. Our description is valid as long as the activity decorrelation time is larger than the time scale of thermal noise.

An isolated active dumbbell exhibits a stochastic trajectory and at long times diffuses in both translation and orientation. In this case, the orientational decorrelation of the active force arises solely from the thermal noise experienced by the monomers. At low temperatures and densities, the thermal noise is inefficient in decorrelating the orientation of the active force. In this case, torques generated by interparticle collisions help orientational decorrelation [7], leading to a decrease in the decorrelation time with increasing density. The single-particle trajectory in the dilute limit ($\rho = 0.1$) at $T = 0.5$ in the presence of active forcing ($f = 5$) clearly shows stochasticity in both translation and orientational displacements [Fig. 1(b)]. The measured translational and rotational MSD in this dilute limit show enhanced diffusion with active forcing (Fig. 2).

B. Active dumbbells at high density

As the density is increased further, steric effects that hinder the rotation of a dumbbell cause the decorrelation time to

increase with increasing density. Only the second regime in which the decorrelation time increases with increasing density is observed when the temperature is high; see Fig. 1(c). This is consistent with dense assemblies of active particles, both in the cellular and granular context, where both local alignment and orientation decorrelation times are strongly influenced by cell-cell (intergrain) contact interactions [16,26].

Note that there are no ad hoc alignment rules and there is no *externally prescribed activity decorrelation time*. Rather, both the local alignment and orientational decorrelation time at high densities emerge from thermal fluctuations on the constituent monomers comprising each dumbbell and collisions driven by thermal and active forces, an emergent many-particle feature. As a corollary, *both the local alignment and orientational decorrelation time are functions of temperature, density, and activity*. Figure 1(c) shows the rotational relaxation time τ_α^R for different densities at two different temperatures for a self-propulsion force, $f = 10.0$. At high densities and fixed (low) temperature, the orientational decorrelation time increases with decreasing f , and it diverges as the glass transition is approached from above.

As T or f is decreased starting from the liquid phase at high T and f , the MSD [Figs. 3(b) and 3(c)] begins to show cage diffusion, with a distinct intermediate plateau and a reduced late time diffusion coefficient, characteristic of the approach

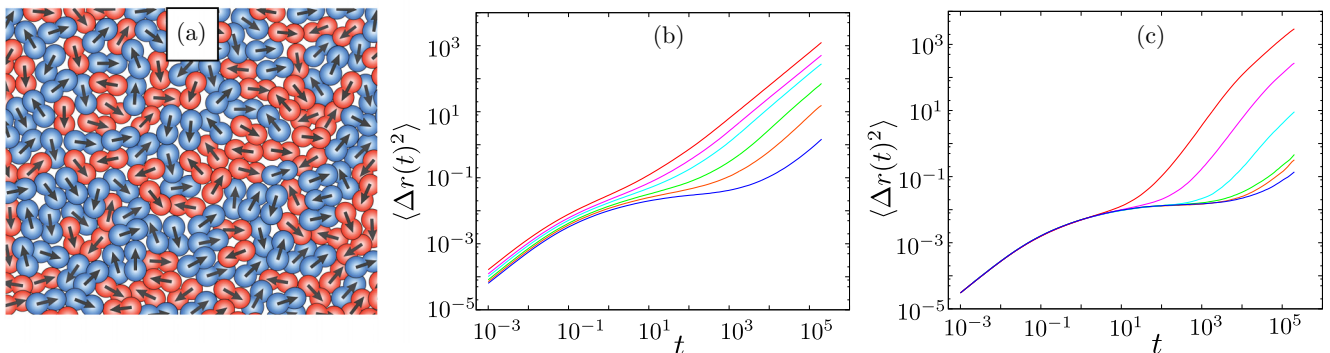


FIG. 3. (a) A dense binary assembly of self-propelled dumbbells of A (blue) or B (red) type. (b),(c) Mean-square displacement [$\langle \Delta r(t)^2 \rangle$] as function of time t : (b) for propulsion force $f = 2.0$ for different temperatures $T = 3$ (blue), 3.5 (orange), 4 (green), 5 (cyan), 6 (magenta), and 8 (red); and (c) for temperature $T = 1.5$ for different propulsion forces $f = 3$ (blue), 3.5 (orange), 4 (green), 5 (cyan), 6 (magenta), and 8 (red).

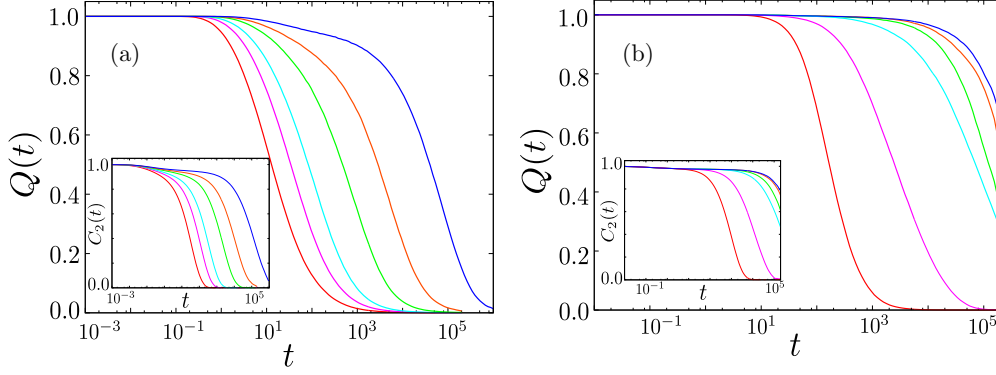


FIG. 4. (a) Overlap function, $Q(t)$, measured for propulsion force $f = 2$ at different temperatures $T = 3$ (blue), 3.5 (orange), 4 (green), 5 (cyan), 6 (magenta), and 8 (red); and (b) for temperature $T = 1.5$ at different propulsion forces $f = 3$ (blue), 3.5 (orange), 4 (green), 5 (cyan), 6 (magenta), and 8 (red). The inset shows the rotational time correlation function, $C_2(t)$, and its behavior for the same set of parameters in both cases.

to a glass. This is accompanied by a slowing down of both the translational and rotational structural relaxation process, captured by the two-step decay of the correlation functions, $Q(t)$ and $C_2(t)$ [Figs. 4(a) and 4(b)]. Thus, the corresponding α -relaxation times τ_α^T and τ_α^R increase, as T or f decreases (Fig. 5). As is usual in studies of glass-forming systems, we estimate the glass-transition temperature, separately for both rotational and translational relaxation, by fitting the respective α -relaxation time to a Vogel-Fulcher-Tammann (VFT) form, $\tau_\alpha = \tau_\infty \exp[\frac{1}{\kappa(\frac{T}{T_{\text{VFT}}}-1)}]$, where τ_∞ is the relaxation time at large temperatures, κ is the coefficient of kinetic fragility, and $T_{\text{VFT}}(f)$ is the putative glass-transition temperature for an applied active force f . The resultant phase diagram in the T - f plane, obtained by marking the different $T_{\text{VFT}}(f)$ values, is shown in Fig. 6. We find that the rotational and translational degrees of freedom freeze-out from the liquid at different $T_{\text{VFT}}(f)$, resulting in two distinct glass phases, namely translational glass (TG) and translational-rotational glass (TRG).

The phase diagram itself does not reveal any difference between approaching the glass by lowering T or f . To see differences in the active and passive systems, distinguished by their Peclet number, one needs to probe their dynamical

heterogeneity. Already, the VFT fits give some hint of this: the kinetic fragility (κ) of translational glass shows a decrease with increasing activity f ; see Fig. 7(a). A similar behavior is also observed for the rotational relaxation [Fig. 7(b)]. Thus, the active glass becomes *stronger* or less *fragile* than a passive glass, both during translational and rotational arrest. The decrease in fragility in an active soft supercooled liquid is consistent with some earlier numerical [5] and theoretical [28] studies. We will see later how this result is also consistent with observations in reconstituted epithelial tissues that have been reported to show glassy behavior [29].

C. Vortices and dynamical heterogeneities in the vicinity of dynamical arrest

To explore the difference in behavior while approaching the arrested state by either decreasing T or f , we probe the dynamics in finer detail at specific points along an iso-relaxation-time ($\tau_\alpha^T = 102.85$) line (Fig. 6), which lies in the supercooled liquid regime. We measure the displacement field vectors of the center of mass of the dumbbells, $\mathbf{d}(\mathbf{r})$, over a time τ_α^T , and we construct a spatial map of corresponding streamlines, which are shown in the left panel of Fig. 8. For the passive system ($f = 0$), such a map is structureless with no large-scale

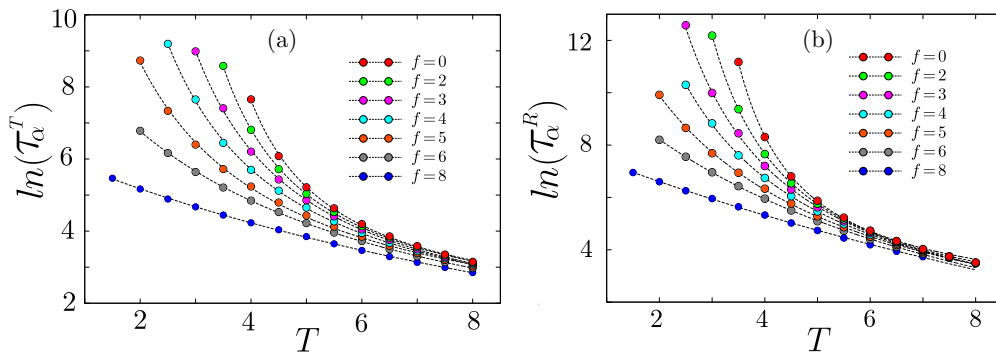


FIG. 5. (a) Translational α -relaxation time scale (in filled circles) as a function of temperature (T) for different values of self-propulsion force [$f = 0$ (red), 2 (green), 3 (magenta), 4 (cyan), 5 (orange), 6 (dark gray), and 8 (blue)]. The black dotted lines represent the fitting of the data sets for each f to the VFT form. (b) Rotational α -relaxation time scale (in filled circles) τ_α^R vs T for different values of f , with fits (black dotted lines) to the VFT form.

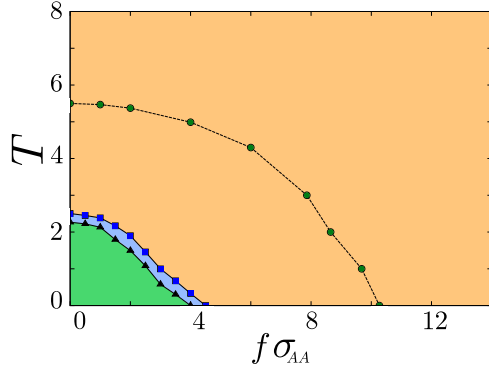


FIG. 6. Phase diagram in the $(T-f)$ plane shows a liquid (L, brown), translational glass (TG, blue), and translational-rotational glass (TRG, green) with phase boundaries determined from VFT fits. The dashed line represents the iso-relaxation-time ($\tau_\alpha^T = 102.85$) line, along which the dynamics is probed at points marked in green.

spatial correlation, Fig. 8(b) (left panel). On increasing Pe along the iso- τ_α^T line, one begins to observe distinct *vortexlike* structures, whose size increases with increasing Pe, as seen in Fig. 8(a) (left panel). This pattern (or lack of it in the passive case) is also quantified via the coarse-grained vorticity $\omega(\mathbf{r}) = \nabla \times \mathbf{v}_\tau(\mathbf{r})$, where $\mathbf{v}_\tau(\mathbf{r}) \equiv \mathbf{d}(\mathbf{r})/\tau_\alpha^T$, which is shown using the color maps in the left panels of Fig. 8. This differs from the usual definition based on instantaneous velocities and reflects the fact that the dynamics in the supercooled regime manifests only over α -relaxation times. Further, in the right panel of Fig. 8, we show spatial maps of the magnitude of single particle displacements during τ_α^T to gauge the extent of dynamical heterogeneity exhibited in either situation. The active system, Fig. 8(a) (right panel), has much more spatial heterogeneity in dynamics than the passive one, Fig. 8(b) (right panel). Also, notice the anticorrelation in the vorticity and the magnitude of particle displacement: regions with low (high) vorticity correspond to fast (slow) dumbbells. Particles between a vortex-antivortex pair are faster, while particles in the vortex core are slower.

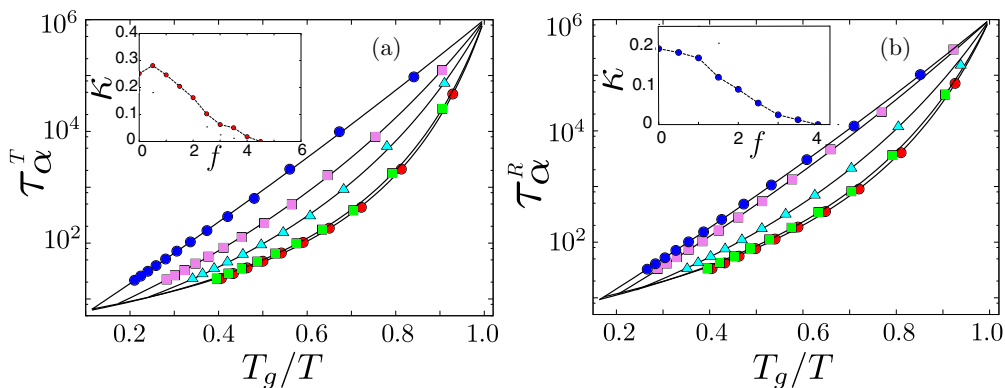


FIG. 7. Angell plots: (a) Variation of translational relaxation times τ_α^T vs scaled temperature (T/T_g) at different values of the active force. As in [27], T_g is defined as the temperature at which $\tau_\alpha^T = 10^6$. The inset shows how the corresponding kinetic fragility κ decreases with increased self-propulsion force. (b) Variation of rotational relaxation times τ_α^R vs scaled temperature (T_g/T) with changing active force: $f = 0$ (red), 1 (green), 2 (cyan), 3 (violet), and 3.5 (blue). T_g is defined as the temperature at which $\tau_\alpha^R = 10^6$. The inset shows how the corresponding kinetic fragility κ decreases with increased self-propulsion force.

Vortices also appear in the dynamics of spherical active particles—this was observed in [2], though not analyzed. To contrast the behavior of anisotropic with spherical active particles, we study the dynamics of a dense assembly of spherical self-propelled particles in two dimensions, interacting via an LJ potential (Kob-Andersen model), subject to a thermal noise with temperature T and an active noise whose variance is f^2 and correlation time is τ_p . We find that indeed vortices are observed, however these appear only when the persistence time τ_p is large (Fig. 9). In particular, swirls do not appear when one is away from the glass transition or when τ_p is low (Fig. 9). In contrast, large swirls and vortices appear generically in an active supercooled liquid of dumbbells characterized by a high Péclet number. Making the particles anisotropic and allowing the decorrelation time to emerge as we have done here makes the regime over which swirls are observed larger, allowing us to make quantitative estimates of length scales and follow their dependence on control parameters, as we do below.

To extract correlation lengths from the spatial structures visible in such maps, we calculate the angle-averaged correlation functions of (i) the orientation of the displacement vectors of the dumbbell, $C(r) = \langle 2 \cos^2 \Delta\theta(\mathbf{r}) - 1 \rangle$, where $\Delta\theta(\mathbf{r})$ is the angular separation between two displacement vectors separated by distance \mathbf{r} [Fig. 10(a)], and (ii) the vorticity, $G(r) = \langle \omega(\mathbf{0})\omega(\mathbf{r}) \rangle$, evaluated over τ_α^T [Fig. 10(b)]. The extracted correlation lengths, ζ and χ , respectively, show a crossover as we move along the iso- τ_α^T line, and they distinguish the passive (low Pe) from the active (high Pe) supercooled liquids; see Fig. 11(a).

If we now move toward the dynamically arrested regime from either extreme ends, i.e., along the passive direction (Pe = 0) where the active forcing is absent, or the athermal active direction (Pe = ∞) where thermal fluctuations are suppressed, we clearly observe the stark differences in the way the above-mentioned spatial correlations grow. As one goes toward the glass transition at Pe = 0, there is no significant change in the correlation lengths ζ and χ , which continue to remain at the scale of the dumbbell [Fig. 11(c)]. There is of course the usual dynamical heterogeneity associated with the emergence and growth of *fast* moving and *slow* moving

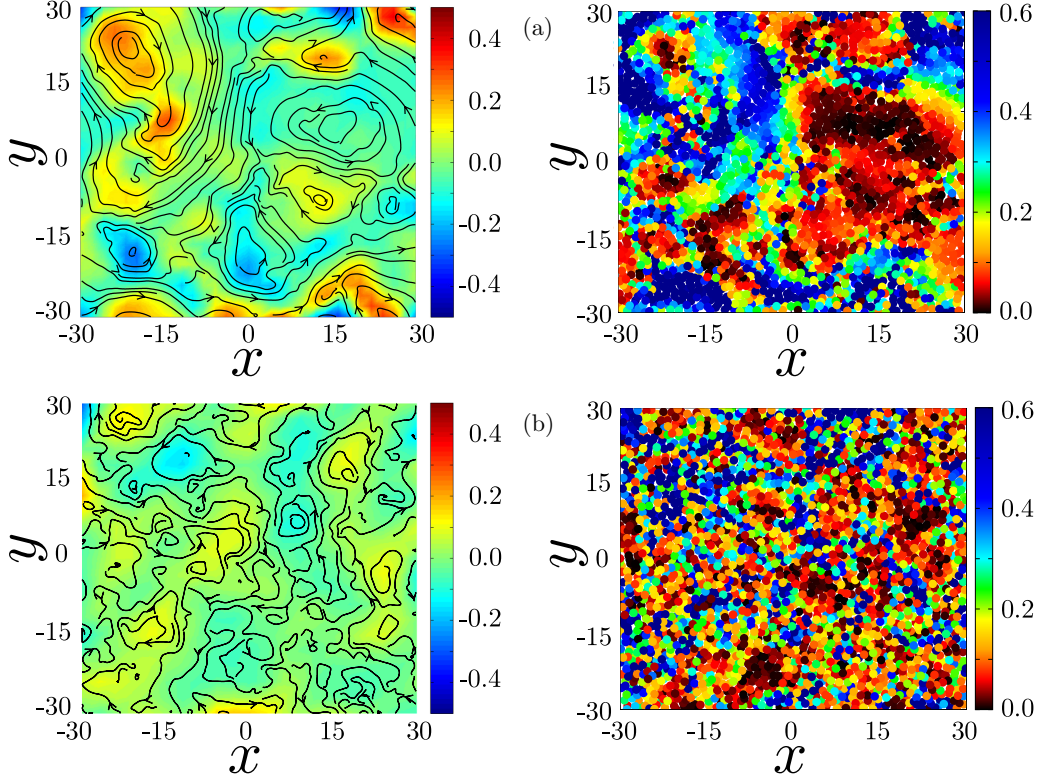


FIG. 8. (a) Left: Streamlines of displacement field, $\mathbf{d}(\mathbf{r})$, for the active dumbbells ($f = 10.3$, $T = 0$) computed over $t = \tau_\alpha^T$ showing large vortexlike structures with the underlying color map reflecting the corresponding values of the vorticity $\omega(\mathbf{r})$. Right: Map showing the magnitude of displacement during $t = \tau_\alpha^T$, illustrating the extent of heterogeneous dynamics in the active glass, with blue particles being the fastest and black particles being the slowest. Note that the vorticity and particle velocities are *anticorrelated* (see the text). (b) Left: Streamlines of displacement for passive dumbbells ($f = 0$, $T = 5.5$) along with the corresponding vorticity color map. Right: Displacement map for the passive liquid. Note the absence of any large-scale structures and the resultant low vorticity.

domains [30] and the corresponding increase in relaxation times [25,31]. However, on approaching the glass transition from the active side, along ($\text{Pe} = \infty$), the nature of the dynamical heterogeneity is very different and is associated with

swirling or vortex patterns that grow in size. The corresponding growing length scales [Fig. 11(b)] go as $1/\sqrt{f - f^*}$, far away from the glassy regime ($f^* = 4.5$), and cross over to $1/(f - f^*)$ as one nears dynamical arrest.

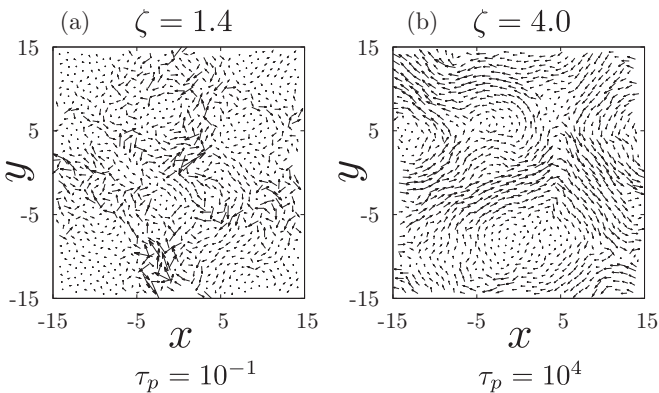


FIG. 9. Displacement field for an athermal assembly of a binary LJ mixture of disks (Kob-Andersen model), computed over time scales of corresponding $\tau_\alpha \approx 5028$, for two different persistence time scales: left, $\tau_p = 10$; and right, $\tau_p = 10^4$, for applied active forcing of $f = 3.5$ and 1.28 , respectively, illustrating that the swirls become large only when persistence time scales are large, as indicated by the measured correlation lengths (ζ).

IV. HYDRODYNAMIC CALCULATION

To understand the origin of these vorticity scales, we construct a hydrodynamic description of the self-propelled dumbbells in the isotropic phase. Our simulations show that the velocity \mathbf{v}_τ is correlated with the orientation of dumbbell \mathbf{n} , or more precisely $\mathbf{Q} \cdot \mathbf{f}$, where \mathbf{Q} is the nematic orientation tensor describing the apolar orientation of the dumbbell and \mathbf{f} is the body-attached propulsion force. This correlation increases with the Peclet number along the iso- τ_α^T -line before saturating due to packing considerations (Fig. 12). This suggests that the appropriate hydrodynamic fields are the conserved densities, the orientation tensor \mathbf{Q} , and the dumbbell velocity \mathbf{v} .

The fact that it is a two-component system just goes toward forming a translational and orientational glass—it is not relevant to the generation of the large swirls or vortices. We will therefore treat it as a one-component system with a single conserved density field ρ , whose dynamics is given by

$$\partial_t \rho + \nabla \cdot (\rho \mathbf{v}) = 0. \quad (3)$$

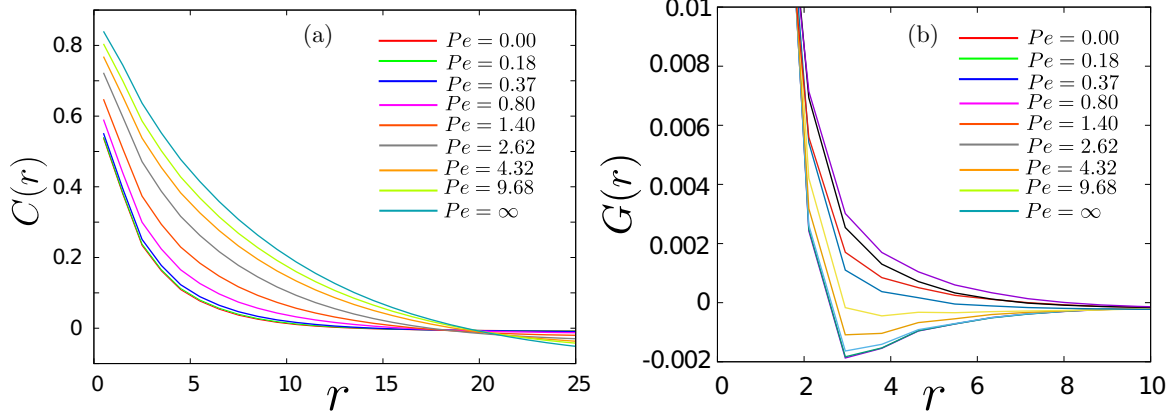


FIG. 10. (a) Spatial correlation function of the orientation of the displacement vectors of the center of mass of the dumbbells, $C(r) = \frac{1}{2\pi} \int \langle 2 \cos^2 \Delta\theta(\mathbf{r}) - 1 \rangle d\phi$, where $\Delta\theta(\mathbf{r})$ is the angular separation between two displacement vectors separated by distance r . The simulation points are chosen along an iso- τ_α^T line on the $(T-f)$ phase diagram. The correlation length ζ is extracted using the condition $C(\zeta) = 1/e$. (b) Spatial correlation of the vorticity field of the coarse-grained velocity vectors $G(r) = \frac{1}{2\pi} \int \langle \omega(\mathbf{0})\omega(\mathbf{r}) \rangle d\phi$ over a time scale of τ_α^T . The simulation points are chosen along an iso- τ_α^T line on the $(T-f)$ phase diagram. The correlation length χ is extracted using the condition $G(r) = 0$.

Newton's second law provides the equation for the dumbbell velocity \mathbf{v} ,

$$\rho \partial_t \mathbf{v} = -(\Gamma - \eta \nabla^2) \mathbf{v} - \zeta_c \nabla \rho + \nabla \cdot \sigma. \quad (4)$$

Γ represents frictional damping and η is the viscosity associated with the transfer of momentum arising from collisions.

The second term on the right may be thought of as a pressure term arising from density inhomogeneities; ζ_c is therefore a compressibility. The last term on the right is the contribution to the force coming from the total deviatoric stress σ . The total deviatoric stress, $\sigma = \sigma^{\text{op}} + \sigma^{\text{act}}$, is a sum of the order parameter stress, $\sigma^{\text{op}} = \Lambda(\delta F/\delta \mathbf{Q}) - [\mathbf{Q} \cdot (\delta F/\delta \mathbf{Q}) - (\delta F/\delta \mathbf{Q}) \cdot \mathbf{Q}]$ [24], derived from a free-energy functional for the

nematic,

$$F[\mathbf{Q}] = \int d\bar{x} \left[\frac{A}{2} \mathbf{Q}^2 + \frac{C}{4} \mathbf{Q}^4 + \frac{K}{2} (\nabla \mathbf{Q})^2 \right], \quad (5)$$

and the active stress $\sigma^{\text{act}} = fI\mathbf{Q}$ [32]. From this we get

$$\delta F/\delta \mathbf{Q} = \left[\left(A + \frac{C}{2} S^2 \right) \mathbf{Q} - K \nabla^2 \mathbf{Q} \right], \quad (6)$$

where S is the magnitude of the nematic order parameter present in the system and $S^2 = 2 \text{Tr}(\mathbf{Q}^2)$.

In the high-density phase at the onset of glassy behavior, one might choose to ignore spatial inhomogeneities of the density. There are, however, nontrivial temporal correlations of the

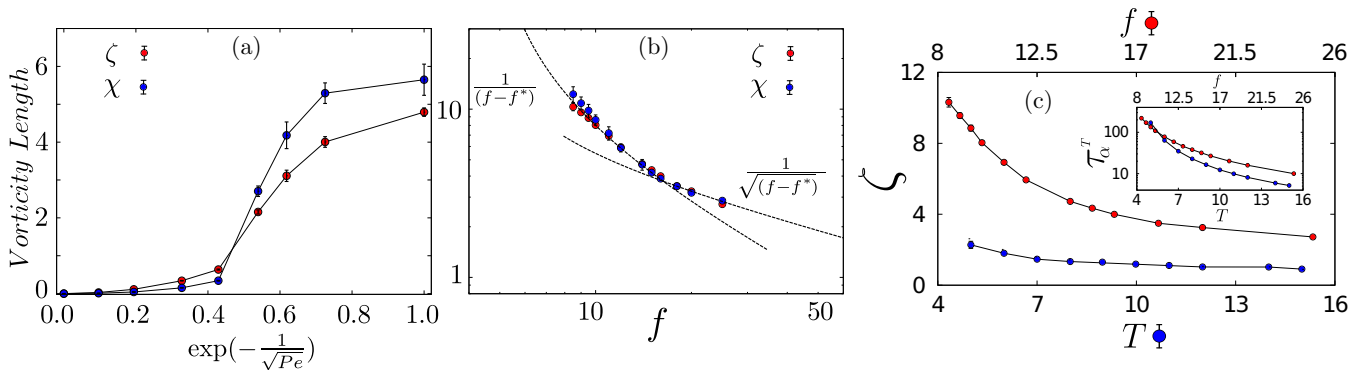


FIG. 11. (a) Correlation lengths ζ , characterizing the degree of alignment of the displacement vectors, and χ , characterizing the spatial correlation of vorticity, as a function of Pe , along the iso- τ_α^T line, show a crossover from a passive to an active supercooled liquid. To highlight the change, we subtract from the measured correlation lengths a microscopic length associated with the size of the dumbbell. The choice of plotting against $\exp[-1/\sqrt{Pe}]$ ensures uniform spacing for the simulation data points over the range of Pe . (b) ζ and χ as functions of activity f at $T = 0$ show an increase and crossover from $1/\sqrt{f-f^*}$ dependence at large f to $1/(f-f^*)$ dependence close to the glass transition at $f^* = 4.5$ (dashed line shows fit). (c) Length scale (ζ) associated with spatial correlation of the direction of the displacement vectors for the dumbbell system at $f = 0$ for different T (blue) and at $T = 0$ for different f (red), i.e., when we approach the glass boundary along two different axes. The correlation length scale does not show any significant change if the glass transition is approached by reducing temperature, but it shows an increase as the system approaches a glass transition by reducing the activity. The inset shows the relaxation time scale (τ_α^T) for a similar set of simulation points at $f = 0$ for different T and at $T = 0$ for different f .

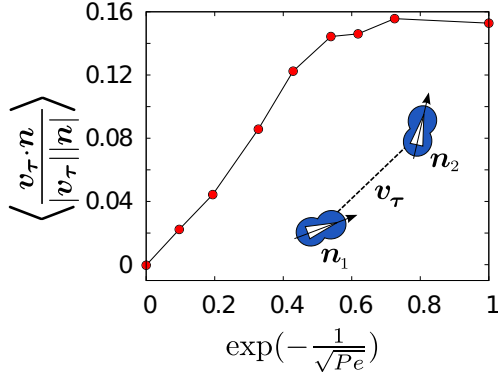


FIG. 12. Average of the normalized dot product of the coarse-grained velocity (\mathbf{v}_τ) of each dumbbell and its average orientation vector ($\mathbf{n} = \frac{\mathbf{n}_1 + \mathbf{n}_2}{2}$) over the α -relaxation time (τ_α^T) as we move through different points on the iso- τ_α^T line from passive to active supercooled liquid region. For a few initial points the correlation between displacement and orientation increases and then it saturates as maximum coupling between these two is reached, which is limited by the packing of the dumbbells.

density, but since we only want to extract the swirling behavior, we ignore this. This allows us to consider the dynamics of \mathbf{Q} and \mathbf{v} alone. The dynamics of \mathbf{v} reduces to

$$\rho \partial_t \mathbf{v} = -(\Gamma - \eta \nabla^2) \mathbf{v} + \nabla \cdot \boldsymbol{\sigma}. \quad (7)$$

The dynamics of \mathbf{Q} is given by

$$D_t \mathbf{Q} = \lambda \mathbf{U} + \mathbf{Q} \cdot \boldsymbol{\Omega} - \boldsymbol{\Omega} \cdot \mathbf{Q} - \gamma^{-1} \frac{\delta F}{\delta \mathbf{Q}}, \quad (8)$$

where D_t represents the convective derivative in the comoving frame, λ is the stable-flow alignment parameter, γ is the rotational viscosity, and \mathbf{U} and $\boldsymbol{\Omega}$ are the symmetric and antisymmetric strain-rates: $\mathbf{U} = \frac{1}{2}[(\nabla \mathbf{v}) + (\nabla \mathbf{v})^T]$ and $\boldsymbol{\Omega} = \frac{1}{2}[(\nabla \mathbf{v}) - (\nabla \mathbf{v})^T]$.

Now linearizing about the isotropic state with no flow, we obtain

$$\dot{\mathbf{Q}} = \frac{\lambda}{2}[(\nabla \mathbf{v}) + (\nabla \mathbf{v})^T] - \frac{1}{\gamma}[A - K \nabla^2] \mathbf{Q}, \quad (9)$$

$$\dot{\boldsymbol{\omega}} = -(\Gamma - \eta \nabla^2) \boldsymbol{\omega} + [\Lambda(A - K \nabla^2) + fl] \nabla \cdot \mathbf{Q}. \quad (10)$$

Taking the curl of the above equations gives us the equation for the vorticity $\boldsymbol{\omega}$.

The lengths scales associated with the spatial patterning of the vortex flows can be obtained using dimensional analysis by balancing the relevant contributions to the stress appearing in Eq. (10).

Away from the glass transition, patterning is generated by balancing the active stress ($fl\mathbf{Q}$) against the orientational elastic stress ($\Lambda K \nabla^2 \mathbf{Q}$). This gives a length scale $\sqrt{\Lambda K / fl}$, consistent with the scaling observed in our simulations at large f [Fig. 11(b) and [33]].

On approaching the glass transition $f = f^*$, the translational motion becomes sluggish and finally arrested. As long as $f > f^*$, the system is still an active *fluid*, and it flows over a time scale τ_α^T . We thus argue that we should still be able to use the active fluid equations, Eqs. (9) and

(10), as long as we renormalize time by $t \rightarrow t/\tau_\alpha^T$. In this highly viscous fluid regime, the patterns are generated by balancing the active stress ($fl\mathbf{Q}$) with the viscous stress ($\eta \nabla \mathbf{v}$). Note that the velocity scale that appears in the balance above is the coarse-grained velocity \mathbf{v}_τ . From our simulations, the typical magnitude of \mathbf{v}_τ is of order l in units of this scaled time. Using this, we get the length scale for the spatial patterning of the velocity to go as $\eta/(f - f^*)$ as long as f is greater than, but close to, f^* [Fig. 11(b)]. The crossover between these two behaviors occurs at a propulsion force $\propto \eta^2 l / \Lambda K$.

Thus, the predictions of the hydrodynamic model completely match the results of our numerical simulations, thus providing insight into the dynamics of a dense assembly of active anisotropic particles.

V. DISCUSSION

In this paper, we study a dense assembly of self-propelling soft anisotropic particles subject to Brownian noise. Our model is distinct from other models that have been studied in that there is no explicit activity decorrelation time nor imposed orientational alignment; these emerge, however, from the collective dynamics of the particles. We observe that this active dense system undergoes two dynamical arrests, first for translational degrees of freedom followed by the rotational degrees of freedom, with an onset that depends on activity. We also demonstrate that the active forcing makes the corresponding supercooled fluid less fragile for both degrees of freedom, and more importantly the heterogeneous dynamics observed in the active fluid is very different from its passive counterpart, exhibiting large-scale swirls and vortices. We further show that in the athermal ($T = 0$) limit, the correlation lengths associated with these spatial structures grow with decreasing active forcing and appear to diverge as the dynamics becomes arrested. We rationalize the occurrence of such length scales and predict their growth and divergence using a continuum hydrodynamic theory of active dumbbells.

Our study of dynamical heterogeneities in active glass composed of anisotropic particles has implications for the collective cell dynamics in epithelial layers. This can be seen by constructing a Voronoi tessellation around each dumbbell; the resulting pattern then resembles an epithelial sheet (see supplementary movie 1,2 [34]). One of the first studies of glassy dynamics close to the jamming transition in a reconstituted epithelial sheet [29] revealed two striking features: (i) the epithelial glass was significantly less fragile compared to a conventional hard-sphere glass, and (ii) systematically reducing cell motility by treatment with titrated amounts of actin depolymerization agents rendered the epithelial sheet more fragile. Our result on how active propulsion makes the dynamically arrested state stronger or less fragile is entirely consistent with this. In addition, our work suggests the possibility of observing large-scale swirls in situations in which cellular propulsion is high and the cell-substrate adhesion is weak [35].

The swirling patterns or vortex structures that we observe for dense assemblies of anisotropic particles are reminiscent of the dynamical patterns seen in *active turbulence* exhibited by

a collection of fluid of active rods [9,10,24]. Is the dynamical heterogeneity exhibited by the active glass a frozen memory of its turbulent past? Our work shows unambiguously that an active glass is fundamentally distinct from a conventional glass.

ACKNOWLEDGMENTS

We thank A. Das, J. P. Banerjee, S. S. Ray, and S. Sastry for useful discussions. R.M. and P.J.B. acknowledge financial support from CSIR, India, and C.D. from DST, India.

-
- [1] L. Berthier and J. Kurchan, *Nat. Phys.* **9**, 310 (2013).
 - [2] L. Berthier, *Phys. Rev. Lett.* **112**, 220602 (2014).
 - [3] R. Ni, M. A. C. Stuart, and M. Dijkstra, *Nat. Commun.* **4**, 2704 (2013).
 - [4] S. Henkes, Y. Fily, and M. C. Marchetti, *Phys. Rev. E* **84**, 040301(R) (2011).
 - [5] R. Mandal, P. J. Bhuyan, M. Rao, and C. Dasgupta, *Soft Matter* **12**, 6268 (2016).
 - [6] E. Flenner, G. Szamel, and L. Berthier, *Soft Matter* **12**, 7136 (2016).
 - [7] L. F. Cugliandolo, G. Gonnella, and A. Suma, *Phys. Rev. E* **91**, 062124 (2015).
 - [8] C. Tung, J. Harder, C. Valeriani, and A. Cacciuto, *Soft Matter* **12**, 555 (2016).
 - [9] H. H. Wensink, J. Dunkel, S. Heidenreich, K. Drescher, R. E. Goldstein, H. Löwen, and J. M. Yeomans, *Proc. Natl. Acad. Sci. (USA)* **109**, 14308 (2012).
 - [10] H. H. Wensink and H. Löwen, *J. Phys. Condens. Matter* **24**, 464130 (2012).
 - [11] J. T. Siebert, J. Letz, T. Speck, and P. Virnau, *Soft Matter* **13**, 1020 (2017).
 - [12] D. F. Hinz, A. Panchenko, T. Y. Kim, and E. Fried, *Comput. Phys. Commun.* **196**, 45 (2015).
 - [13] R. A. Simha and S. Ramaswamy, *Phys. Rev. Lett.* **89**, 058101 (2002).
 - [14] Y. Hatwalne, S. Ramaswamy, M. Rao, and R. A. Simha, *Phys. Rev. Lett.* **92**, 118101 (2004).
 - [15] A. P. Solon, Y. Fily, A. Baskaran, M. E. Cates, Y. Kafri, M. Kardar, and J. Tailleur, *Nat. Phys.* **11**, 673 (2015).
 - [16] J. A. Park *et al.*, *Nat. Mater.* **14**, 1040 (2015).
 - [17] D. Bi, J. H. Lopez, J. M. Schwarz, and M. L. Manning, *Nat. Phys.* **11**, 1074 (2015).
 - [18] G. Lambert, A. Bergmann, Q. Zhang, D. Bortz, and R. Austin, *New J. Phys.* **16**, 045005 (2014).
 - [19] N. Kumar, H. Soni, S. Ramaswamy, and A. K. Sood, *Nat. Commun.* **5**, 4688 (2014).
 - [20] W. Kob and H. C. Andersen, *Phys. Rev. Lett.* **73**, 1376 (1994).
 - [21] S. H. Chong, A. J. Moreno, F. Sciortino, and W. Kob, *Phys. Rev. Lett.* **94**, 215701 (2005).
 - [22] A. J. Moreno, S. H. Chong, W. Kob, and F. Sciortino, *J. Chem. Phys.* **123**, 204505 (2005).
 - [23] S. H. Chong and W. Kob, *Phys. Rev. Lett.* **102**, 025702 (2009).
 - [24] L. Giomi, *Phys. Rev. X* **5**, 031003 (2015).
 - [25] S. Karmakar, C. Dasgupta, and S. Sastry, *Proc. Natl. Acad. Sci. (USA)* **106**, 3675 (2009).
 - [26] C. Malinverno *et al.*, *Nat. Mater.* **16**, 587 (2017).
 - [27] S. Chakrabarty, S. Karmakar, and C. Dasgupta, *Sci. Rep.* **5**, 12577 (2015).
 - [28] S. K. Nandi and N. S. Gov, [arXiv:1605.06073](https://arxiv.org/abs/1605.06073) (cond-mat.soft).
 - [29] E. H. Zhou *et al.*, *Proc. Natl. Acad. Sci. (USA)* **106**, 10632 (2009).
 - [30] L. Berthier and G. Biroli, *Rev. Mod. Phys.* **83**, 587 (2011).
 - [31] S. Karmakar, C. Dasgupta, and S. Sastry, *Annu. Rev. Condens. Matter Phys.* **5**, 255 (2014).
 - [32] M. C. Marchetti *et al.*, *Rev. Mod. Phys.* **85**, 1143 (2013).
 - [33] E. J. Hemingway, P. Mishra, M. C. Marchetti, and S. M. Fielding, *Soft Matter* **12**, 7943 (2016).
 - [34] See supplemental material at <http://link.aps.org/supplemental/10.1103/PhysRevE.96.042605> for supplementary movies.
 - [35] T. E. Angelini *et al.*, *Proc. Natl. Acad. Sci. (USA)* **108**, 4714 (2011).